Combustion-assisted synthesis of Mn-rich cathode for high performance Li-ion batteries

Prettencia L[a] Soundarrajan E[a] Shanmugharaj AM[b], Kalaivani RA[a]*, Raghu S[b]*

[a] *Department of Chemistry, Vels Institute of Science, Technology & Advanced Studies (VISTAS), Chennai, Tamilnadu, 600 117, India.*

[b] *Centre for Advanced Research and Development - Chemistry, Vels Institute of Science, Technology & Advanced Studies (VISTAS), Chennai, Tamilnadu, 600 117, India.*

* Corresponding author: Email: subraghu_0612@yahoo.co.in; rakvani@yahoo.co.in

Abstract:

The present decade of research is making significant efforts to develop lithium battery technology with stable cycling, high capacity, and affordability. Mn-rich layered materials are likely to fall within this research pace as an effective alternative. However, the life expectancy of Mn-rich layered materials are unpredictably short which impedes its commercial applicability. Herein, we demonstrate the synthesis of Li $[Li_{0.1}Ni_{0.3}Mn_{0.7}]O_2$ by co-precipitation method followed by rapid combustion with organic fuels at various temperatures. Physical characterizations were performed to confirm the structure and surface morphology of Li $[Li_{0.1}Ni_{0.3}Mn_{0.7}]O_2$. The fine-tuned cathode material established stable cycling even at high voltage (4.8V) with the capacity retention of 98.2% upto 100 cycles. The maximum electrochemical rate capabilities at 0.1C, 0.2C, 0.5C, 1C, 2C and 5C are 325 , 314 , 259, 228, 173 and 109 mAh g^{-1} respectively. Thus, Mn- rich cathodes in lithium-based batteries provides a pathway to facilitate practical feasibility, boost cycling stability, attain high-capacity with lower expense.

Keywords:

Lithium–ion battery, Mn–rich cathode material, Co-precipitation method, Rapid Combustion, Capacity variation.

1. Introduction:

Owing to the emergent adoption of electric vehicles and grid energy storage devices, the want for lithium batteries with high energy density, specific capacity, cycling stability, and advanced performance levels has grown enormously. At present, alternative cathode layered materials employing various metal oxide combinations are entering into the platform of commercialization despite their disabilities in practical application [1,2]. Among them layered Ni-rich electrodes have been proposed as potential electrode materials of interest due to their high reversible nature, efficient redox behaviour, and cost-effectiveness. However, cathode materials with Ni content less than 60% encounter numerous challenges with respect to their powder properties and electrode manufacturing methods [3]. Consequently, in the recent years researchers are fascinated towards Mn-based Li-rich cathode layered materials due to their superior capacities which even exceeds the theoretical value, cost-effectiveness for large-scale production, and eco-friendly approach [4,5]. Layered Mn–rich oxide (LMRO) materials first stated by Thackeray et al. revealed a discharge specific capacity of around 200 $mAhg^{-1}$ could be delivered by the $Li_{2-x}MnO_{3-x/2}$ cathodes. LMRO cathode materials were developed in subsequent years via improving the electrochemical property by modifying their composition, integrating other metal ions into the structure, film forming over the material surface, creating vacancies and interstitial sites, developing additives, and so on [6–8]. Characteristic nature of Mn-oxides depicts that they are structurally versatile compounds which exist in different polymorphs with atomic arrangements having wide interstitial space of 1D tunnel, 2D layers or 3D intersecting channels. They also serve as potential static pillar frames that allows the guest ions to intercalate and de-intercalate easily. Also, it is well known that Mn-oxide structures with oxygen vacancies provide extra active sites for reduction and oxidation reaction. Mn has multiple oxidation states among all other transition metals (+1 to +7) which facilitates its analogous oxides to have enhanced electrochemical activity. Hongge pan et al. stated that

LMRO is made up of two phases, a trigonal $LiMO_2$ with the space group R3m (M = Ni, Co, Mn) and an intergrown monoclinic phased Li_2MnO_3 of space group C2/m [5,9].

Fig.1 represents the formation of $LiMnO_2$ resulting from Li_2MnO_3 and $LiMO_2$. It was observed that the electrochemically less active Li_2MnO_3 was activated by $LiMO_2$ accompanied with a phase transition. After the first loop, Li_2MnO_3 transformed into an electrochemically active $LiMnO_2$ phase while the redox behaviour inverted between Mn^{2+} and Mn^{3+} exhibiting high capacity with good cycling stability. Although $LiMnO_2$ evidences to be a promising cathode there are still many practical challenges. The key problem with $LiMnO_2$ is, it blocks the intercalation or de-intercalation of Li-ions during the phase transformation that occurs on the redox reaction. In Li_2MnO_3, at normal operating voltage (4.1 V) the Mn-ions remain in electrochemically inactive Mn^{4+} oxidation state and this state can exist even before the de-intercalation of Li-ions in the crystal [2,5,10,11]. Also, as reported by Pasero et al. in Li_2MnO_3 low number of O-vacancies lead to the formation of Mn^{3+} which poses a significant risk of dissolution in the electrolyte [12]. Nevertheless, certain drawbacks remain unsolved regarding undesired surface/structure patterns during the electrochemical cycling.

The recent trends in LMRO cathode materials includes high performance $Li\ [Mn_{0.8}Ni_{0.1}Co_{0.1}]\ O_2$ synthesized by oxalate co-precipitation method, with most stable layered structured however the initial discharge was 261.6 $mAhg^{-1}$ with 94.2 % of capacity retention [13].LMRO cathode materials modified with boron bulk doping and carbon surface modification to form B-doping layered @spinel@carbon heterostructure reported to exhibit thermal stability at higher temperature[14]. Recently the elemental doping such as Al, Mg, Ti, F, K., can possibly prevent the cation mixing/TM^+ migration and stabilize the material structure for the better cycling of the battery [2].

The present work involves the synthesis of cobalt-free cathode Li $[Li_{0.1}Ni_{0.3}Mn_{0.7}]O_2$ (LNMO) material via co-precipitation method assisted with rapid combustion. It primarily focusses on the structural modification by employing a new level of metal oxide (1:3:7) ratio. While the unique combustion technique enhanced the irregular porous nature on the cathode material by improving the Li-ion intercalation/de-intercalation sites, the variation of processing temperature contributed essentially for the commendable specific capacity/energy density and cycling stability of Mn-rich cathode material with simple procedures.

2. Experimental Section

2.1 Preparation of LNMO

The precursor solution for the co-precipitation reaction was prepared by dissolving the 70:30 ratio of $Mn(NO_3)_2.6H_2O$ and $Ni(NO_3).6H_2O$ in 20ml of water following which a 30ml of ethanol was gradually added to it. The solution was continuously stirred for about 20 minutes at 500rpm in a continuous stirred tank reactor. After being completely dissolved the solution was fed into a burette. In second step, aqueous solution (200 mL) consisting stoichiometric amounts of 1M K_2CO_3, chelating ($(NH_4)_2CO_3$) and complexing agent (5 % ascorbic acid) was prepared. The precursor solution, fed into the burette was slowly added to the aqueous solution at the rate of 3ml/min assisted with continuous stirring at 400 rpm. Throughout this co-precipitation reaction, the pH of the solution was retained at 11 which was simultaneously checked by automatic pH meter and the temperature was set at 50 ^{o}C. No external acid or base is introduced in order to maintain the pH of the solution. The obtained suspension was filtered and dried at 120^{o}C overnight in a muffle furnace. The resultant powder predominantly containing manganese and nickel metal oxides was manually grounded with the stoichiometric amount of LiOH and 10 wt.% ethylene glycol in a mortar for about 60 min and was decomposed at around 250-380^{o}C. The combusted precursor powder was calcined under an air

environment in three steps as depicted: step-1, temperature was raised from ambient to 450^{o}C at a heating rate of 4^{o}C/min and maintained for 1 hr. In step-2, the temperature was elevated to 600^{o}C at a heating rate of 4^{o}C/min and was maintained for 3 hrs. Step-3, the pre-calcined (600^{o}C) samples were divided into two equal parts and sequentially calcined at two different temperatures (i.e.) 750^{o}C and 900^{o}C for 2 hrs. Finally, the prepared cathode material was immediately quenched in liquid nitrogen and subsequently washed several times to maintain the pH at 7.

2.2 Characterization

The X-ray diffraction patterns were examined in a Bruker D8 advance diffractometer using Cu-Kα radiation in the 2θ range of 10^{o}-80^{o}. The additional structural information was studied using Confocal Raman Microscope-Imagining / Spectrometer (Model-Apollo 300R Make-Witech, Germany). The structure and particle size of the sample were investigated on a Quattro S model field emission scanning electron microscope. Brunauer-Emmette-Teller surface area measurements of the samples were performed by BELSorp Max model BET analyser. The oxidation states of the sample was analysed using an Mg-Kα radiation source in a PHI-5000 Version Probe III multifunctional X-ray Photoelectron Spectrometer.

2.3 Electrochemical test

CR2032 coin cells were used in electrochemical investigations. Chemically synthesized positive electrode LNMO was blended with acetylene black (conducting agent), and polyvinylidene fluoride in a weight ratio of 70:20:10 with N-methyl-2-pyrrolidone. Using an automatic coating unit, the obtained slurry was evenly sprayed onto a thin aluminium sheet with a thickness of 150 mm and vacuum-dried at 120^{o}C for 12 hrs. The obtained electrode material was made into pellets with a diameter of 10 mm (active mass ~3-5 mg) and pressed under 5 MPa for 5 s. Finally, the half cells were assembled using pure lithium metal as

anode and 1M $LiPF_6$ dissolved in EC/DMC/DEC (1:1:1) as electrolyte. The active mass ratio of cathode to anode was kept constant at 1.7:1 ratio. The cells were assembled systematically in an argon-filled glove box (ETELUX Lab 2000) with water and oxygen concentrations of less than 1 ppm. Voltammetry analysis was performed on a Biologic SP300 Electrochemical Work Station. The CV scan rate was $0.01 mVs^{-1}$ and the voltage range was 2.0-4.8 V. Constant current discharge-charge and galvanostatic cycling measurements were done at room temperature on a Neware battery testing system in a 2.0-4.8 V potential window (vs. Li^+/Li) at various rates [15].

3. Result and Discussion

Fig.S1 showed the combustion assisted co-precipitation strategy followed by calcination for the preparation of porous LNMO material. In the co-precipitation process the hydroxide derivatives of nickel $Ni(OH)_2$ and manganese $Mn(OH)_2$ formed during the course of the reaction are converted into porous nickel and manganese oxide (NMO) spheres on pre-calcination. They subsequently transform into Li-rich cathode material (LNMO) on addition of the lithium salt precursor (LiOH) followed by calcination at the desired temperature. However, in conventional co-precipitation processes supressing the formation of irreversible Li_2O during electrochemical cycling is less feasible. On the contrary, our combustion backed co-precipitation method induces more oxygen defects in LNMO resulting by the formation of coated NMO particles which arises due to the interaction of ethylene glycol with the partial lattice oxygen of the NMO spheres Scheme 1. During high temperature calcination under air environment in the presence of lithium precursor the coated ethylene glycol is converted to CO_2. This results in the formation of oxygen defects and subsequent insertion of lithium-ion thereby producing highly porous LNMO particles which is figuratively presented in the Scheme 2 [16–19].

3.1 Structure, morphology and composition analysis

3.1.1 XRD analysis

XRD patterns of LNMO material at three different temperatures are displayed in Fig. 2. The obtained XRD patterns are well matched with the JCPDS-00-052-0457 data, corroborating the rhombohedral geometry with R3m space group, revealing the presence of the layered $LiMO_2$ phases. In addition, co-existence of the weak XRD patterns (2θ = 20^o~25^o) corresponding to the Li_2MnO_3 phases with monoclinic C2/m space groups also exists in the prepared $Li[Li_{0.1}Ni_{0.3}Mn_{0.7}]O_2$ materials. The isolated distinct peaks of $LiMO_2$ and Li_2MnO_3 lattice pattern stipulate that the prepared Li-rich layered oxides have composite structures. [13,18]. The appearance of high refined peaks (003), (104) at 750^{o}C and 900^{o}C indicated that the crystalline nature intensifies at higher temperatures. The existence of weak peak at 2θ=21.5˚ indicated the monoclinic Li_2MnO_3[2,13,14] . Previously reported cathode materials LMR-NMC/LMNCO exhibited two defined peak splits at (006)/(012) and (018)/(110) which confirmed the layered structure but herein when the temperature was increased only the split at (006)/(012) was observed. The spilt at (018)/(110) was present at 600^{o}C but then it gradually disappeared at 750^{o}C and 900^{o}C confirming the material's restructure at high temperatures. Table 1 represented the lattice parameter values a, c, c/a and $I_{(003)}/I_{(104)}$ of the sample treated at different temperatures. The c/a ratio of the all the three samples were greater than 4.9 signifying good lamellar structure while the intensity ratio (R) of I (003)/I (104) exposed that the cation mixing is less than 1.2 for the material treated at 900^{o}C. Larger the intensity ratio (i.e. >1.2) greater is the hexagonal ordering of the lattice. The ratio of the samples treated at 600^{o}C and 750^{o}C were almost equal to the predicted value (1.2). From the tabulated results, it is clearly seen that cation mixing exists at high temperatures which blocks the transition metal migration and triggers the disappearance of the peak spilt at (018)/(110). This validates the existence of spinel along with the layered structure [2,20]. The calcination temperature affects the transition between spinel - layered - spinel. Low temperature calcinated specimens are

dominated by the spinel phase; as Yi Pei et al. previously stated, the phase transition from spinel to layered occurs at temperatures between (500 ºC – 700 ºC); however, at higher temperatures, such as (800 ºC - 900 ºC), the Li is volatilized, increasing the spinel phase content of the specimen. When comparing the results of XRD, Raman shift, and electrochemical performance of samples at different temperatures, we come to the following conclusions.

1. At 600 º C, the prepared sample had the lowest content spinel phase probably the transition should be initiated from spinel to layered, however, the Li insertion is not so facilitated at such temperature, therefore the capacity obtained is low, in addition to it the Li2MnO3 phase is dominantly present at 600 º C.
2. At 750 ºC, the sample has transformed into complete layered phase / very least content of spinel phase with enhanced diffusion of excess Li. The excess Li would gradually insert and compensate Li in spinel phase. The content of layered phase gradually increases with increased temperature. The sample exhibits good electrochemical performance with perfect stability.
3. At 900 ºC, the Li content start to volatilized and layered gradually transforming into spinel. The state where two phase, i.e., layered / spinel exist together evident from Raman spectra. However, the spinel phase is moderate therefore the sample display high capacity beyond theoretical capacity. On the other hand there is considerable amount of cation mixing ensured in XRD and Raman Spectra reduces the stability of the sample.[21,22]. Figure S3: shows comparison of XRD pattern of Li $[Li_{0.1} Ni_{0.3} Mn_{0.7}] O_2$ calcinated at 900 º C, in different cycles.

3.1.2 Raman spectroscopic analysis

The Raman spectra of all the three samples (Fig.3) exhibited two major bands around 490 and 600 cm^{-1} ascribed primarily to the E_{1g} and A_{1g} vibrations of the R3m space group. The weak band around 427 cm^{-1} and 560 cm^{-1} corresponded to the B_g and A_g vibrations of Li_2MnO_3. As the temperature increased, the peak around 427 and 560 cm^{-1} slowly vanished owing to the transmission of Mn^{4+} to Mn^{3+}. It is noticed that Mn^{3+} plays a vital role in enhancing the capacity whereas Mn^{4+} is electrochemically inactive. This occurrence is obseved due to the very low capacity of Li_2MnO_3 phase which is dominantly present at 600ºC. Increased capacities are observed at elevated temperatures because of the enhanced diffusion and better activation of Li_2MnO_3 by $LiMO_2$ ($M=Mn_xNi_y$). Humps around 650 cm^{-1} at 900ºC and 750ºC revealed the reconstrution of phase where the layers are accompanied with spinel phase. But these humps were completely absent for the sample treated at 600ºC [23,24].

3.1.3 FE-SEM analysis

FE-SEM images (Fig.4) gave the structural framework and texture of the material. The sample treated at 900ºC as displayed in Fig.4 (a), (b) ensured sperical ball morphology with extraordinary microporus nature which will lead to enhanced electrochemical property for battery application. Additionally, the spheres had no noticeable aggregation for the LNMO synthesized at 900ºC. The EDX spectrum of LNMO (Fig.4.(c)) showed a dominant Mn peak. The observed value of relative concentration of Ni:Mn closely matches with that of the theoretical composition. Nucleation process has started as indicated in Fig.S2.(a), It specified the formation of nano-sized crystallites from molten material which can be noticed as a phase transformation in the XRD pattern. As shown in Fig.S2.(b), the sample calcinated at 750ºC revealed spherical shape particles with flakes attached to it. It had uniform porous nature and still existed in formation stage. At 900ºC (Fig.S2.(c)) the flakes around the spherical mass began to condense and its porosity became uneven. From Fig.S2 it is seen that the particle size was observed to increase with increasing temperature conditions. Also, the combustion process

had created irregular porosity in the material as reported in the [25,26]. As the temperature increased, the porosity of the sample increased gradually due to the difference in thermal expansion of nearby metal atoms of the composite. Therefore the adsorption capacities increased as the temperature rises [27]. Thus it is validated that the unique synthesis procedure also impacted the property and morphology of the samples.

3.1.4 BET analysis

The parameters such as Brunauer-Emmett-Teller (BET) surface area, total pore volume (V_P), volume of adsorbed nitrogen on the LNMO surface (V_m) and mean pore diameter (D_P) were calculated using the BET nitrogen adsorption-desorption isotherms and their results are included in Table 2. At 600ºC, the surface area of the sample was 9.7 m^2g^{-1} and is directly proportional to the quantity of adsorption and pore volume. The sample treated at 700ºC has surface area of 15.1 m^2g^{-1}. And the surface area of the material at 900ºC was 15.4 m^2g^{-1}. The electrochemical properties are significantly influenced by the increased surface area of the samples. Based on pore inter-connectivity, porosity of the sample also affects the ion diffusion kinetics which is a deciding factor of the rate capacity performance[28–30].

3.1.5 XPS analysis

The samples were subjected to X-ray Photoelectron Spectroscopy in order to identify the oxidative states and local architectural contexts of transition metal ions during the thermal treatment/chemical reaction. Fig.5. showed the XPS spectra of Mn 2p, Ni 2p, Li 1s, and O 1s. In Fig.5.(a) Mn 2p had 2 major peaks, Mn 2p 1/2 at 653.246 eV and Mn 2p 3/2 at 642.228 eV which was consistent with the standard data. For better understanding the 2 major peaks were de-convoluted and they clearly revealed the peaks of Mn^{4+}, Mn^{3+} and Mn^{2+} with its

corresponding peak positions to be 643.02, 641.995, 640.98 eV (Mn 2p 3/2) [2]. In Fig.5.(b) Ni-ions appeared as two major peaks at 855.06 and 872.45 eV with peak difference 17.39 eV which is very close to the reference range 17.24-17.47 eV. On de-convoluting the Ni 2p spectra, the peaks 848.62, 855.06, 861.10, 872.45, 879.26 and 883.04 eV were obtained [31,32]. Therefore, the valence state of Ni-ion is verified as +2. Li-ion (Fig.5.(c)) exhibited only one peak at 54.16 eV and similarly oxygen (Fig.5.(d)) had one major peak at 529.565 eV. Surface hydrations peaks and dissolved/substituted oxygen of the defective site appeared at 531.28 and 527.40 eV respectively. In addition to a regular crystal structure, the dissolved oxygen reacted with the incoming Li-ions to form Li_2O. Thus, Li-ions were consumed by dissolved oxygen of the defective sites which caused initial capacity loss. Later, they fragmented to pair the atomic oxygen with Li and Mn/Ni. This allowed the capacity to raise and maintain a stable performance by occupying the defective site [33,34].

3.2 Electrochemical studies

3.2.1 GCD analysis

Fig.6. showed the charge and discharge curves for LNMO samples at a current density of 0.1C in the voltage range 2.8-4.8V. The samples treated at different temperature showed good cyclic stability. At 600ºC (Fig.6.(a)), the sample exhibited a capacity value of 148 $mAhg^{-1}$-158 $mAhg^{-1}$ in which the Li_2MnO_3 was not activated and the structure of the material was not formed completely [4]. At 750ºC (Fig.6.(b)), the sample unveiled a capacity (240 $mAhg^{-1}$) which was approaching the theoretical capacity (280 $mAhg^{-1}$). It was stable up to 100 cycles and the FE-SEM image also accounted for good porous nature of the sample. In layered Mn-oxides there is a high possibility of exceeding the theoretical capacity (280 mAhg-^{1}) since it depends upon the number of Li-ions exchanged during the redox reaction [5,10]. The maximum capacity achieved was 325 $mAhg^{-1}$ for the sample treated at 900ºC (Fig.6.(c)) which was higher than the theoretical capacity calculated [10]. The low initial capacity discharge for

all the samples can be attributed to two major reasons: (a) Initial Li-ions consumed by non-lattice oxygen/dissolved oxygen and (b) The diffusion that occurs with two phase model in Mn-rich lithium layered oxides. Li-ion diffusion coefficients associated with $LiMO_2$ was considerably larger when compared to those associated with $Li_2MnO_3/LiMnO_2/MnO_2$. Furthermore, the interface activation energy associated with $LiMO_2$ and MO_2 was comparatively small but it was larger for $Li_2MnO_3/LiMnO_2/MnO_2$. Therefore the intercalation of Li-ions is dominated by Li_2MnO_3 [35]. Fig.6.(d) displayed the cyclic stability of all the three samples calcinated at three different temperatures. There was a sudden hike in the charging capacity values of the samples treated at 750^{o}C and 900^{o}C due to the formation of metastable state and it also revealed the increasing irreversible nature of Li_2MnO_3 which electrochemically enhances $LiMnO_2$. The capacity of sample at 900^{o}C started to fade slightly after 86 cycles which exposed the presence of spinel phase along with the layered structure and the cation mixing which is well discussed in XRD and Raman analysis [36]. Fig.7.(a) exhibited the rate performance of LNMO at 900^{o}C under different current (C) rate. The cell was initially charged at 0.1C and discharged at 0.1C, 0.2C, 0.5C, 1C, 2C, 5C and back to 0.1C. Manganese oxides are commonly considered to have low electrical conductivity which is a major disadvantage for achieving higher capacity at high current densities [9]. The material treated at 900^{o}C showed best discharge capacities at 0.1C-325 $mAhg^{-1}$, 0.2C-314 $mAhg^{-1}$, 0.5C-259 $mAhg^{-1}$, 1C-228 $mAhg^{-1}$, 2C-173 $mAhg^{-1}$, 5C-109 $mAhg^{-1}$ and 0.1C-307 $mAhg^{-1}$. When cycled back to 0.1C, the discharge specific capacity of LNMO did not return back to its original capacity reach. This increased irreversibility at low currents indicated the excess removal of Li-ions since the formation of spinel phase could reversibly accommodate Li^+. Low currents allowed slow diffusion and extraction of Li-ions from layered material and led to increased deintercalation/decreased intercalation. However, at high currents the mobility of Li-ions is faster in ejecting out of the accessible sites and inserting them back again. Hence at

0.1C only 94% of retention is assessed due to the structural inconvenience for Li-ion mobility [7]. A comparison specific capacity/ retention values of other conventional methods are tabulated in Table 3.

3.2.2 CV analysis

Fig.7.(b) illustrated the CV profile for LNMO samples between 2 V and 4.8 V at a scanning rate of $0.1 mVs^{-1}$. The area between the redox peaks gradually increased with increasing temperature and ensured the stability of the structure. If the value of $I_{(4.4V)}/I_{(3.9V)}$ is lesser the structure is verified to be highly stable [2]. During the initial charge process, the cathode material displayed two distinct peaks one at 3.9 V corresponding to the Li-ion extraction from the layered $LiMO_2$ framework and the other one at 4.4 V pertaining to the activation process of Li_2MnO_3 on oxidation of Ni^{4+}/Ni^{2+} & Ni^{3+}/Ni^{4+}. The release of Li-ions in the layered Li_2MnO_3 formed LiO_2 resulting in the irreversible loss of oxygen [7,19,44]. The reduction peaks at 3.6 V and 4.1 V corresponded to $Ni^{4+/3+}$ and $Mn^{4+/3+}$. When the charge is below 4.5 V the oxidation state of nickel toggles between +2 and +3. When the charging potential is increased to 4.8 V extraction of Li-ions accompanied by the expulsion of oxygen takes place. The reduction peaks at 3.6 V and 4.1 V are attributed to the reduction of Ni^{4+} and intercalation of lithium into the tetrahedral site of $LiMO_2$ respectively [45,46].

3.2.3 EIS analysis

Fig.7.(c) represented the essence of interfacial electrochemical properties and reaction kinetics of LNMO at varied temperatures. EIS experiment was conducted in the frequency range of 100 kHz-0.01 Hz. At high frequency, a semi-circle was obtained which corresponded to the solid-state interface layer resistance R_{SEI} and at high-intermediate frequency region charge transfer resistance R_{CT} was obtained. The low frequency region had a slope corresponding to the Warburg impedance of the solid phase diffusion. As evidenced from

Table 4, the charge transfer resistance (R_{CT}) and R (CEI) decreased at higher temperatures illustrating that at elevated temperatures LNMO becomes a highly ordered structure which in turn makes the path easy for ion/electron movement and thereby reducing the resistance. The exchange current density (A) also increased at higher temperatures leading to high conductivity.

4. Conclusion

In conclusion, this research has successfully studied the electrochemical efficiency of Li $[Li_{0.05}Ni_{0.3}Mn_{0.7}]O_2$ electrode material synthesized using co-precipitation process assisted with rapid combustion at various temperatures. Structurally stable Mn-rich cathode with high operating voltage (4.8 V) and capacity of 325 $mAhg^{-1}$ at 900°C with long-term cycles has been successfully prepared in comparison with earlier reported results. Taking into account of these results, Li $[Li_{0.05}Ni_{0.3}Mn_{0.7}]O_2$ is proposed as an efficient and safer electrode material for commercial lithium-ion battery applications. The future aspects focus on optimizing certain parameters like synthesis route, temperature, dopant etc to achieve 100% stability at 900°C in the desired cathode material.

ACKNOWLEDGEMENT

We gratefully acknowledge the financial support from (DST/TMD/MES/2K17/39G), New Delhi. The first author is gratefully acknowledging the financial support from VISTAS, Grant Vels Research Fellowship (VRF) and also for all the equipment facility from CARD-Chemistry VISTAS.

The first author expresses deep sense of gratitude to Mr. Santhosh, Research Scholar, Nuclear Physics Department, University of Madras for the fruitful discussion and interpretation on XRD data and also Mr. Irfan, Research Scholar, Department of Chemistry, Vels Institute of

Science, Technology & Advanced Studies (VISTAS), Chennai for the great help rendered in analysing XPS data for the samples.

Reference

[1] P. Vanaphuti, J. Chen, J. Cao, K. Bigham, B. Chen, L. Yang, H. Chen, Y. Wang, Enhanced Electrochemical Performance of the Lithium-Manganese-Rich Cathode for Li-Ion Batteries with Na and F CoDoping, ACS Appl. Mater. Interfaces. 11 (2019) 37842–37849. https://doi.org/10.1021/acsami.9b13838.

[2] C. Song, W. Feng, X. Wang, Z. Shi, Improved storage capability and cycle stability in a Li-riched cathode by substituted Al, J. Electroanal. Chem. 862 (2020) 113962. https://doi.org/10.1016/j.jelechem.2020.113962.

[3] J. Kim, H. Lee, H. Cha, M. Yoon, M. Park, J. Cho, Prospect and Reality of Ni-Rich Cathode for Commercialization, Adv. Energy Mater. 8 (2018) 1–25. https://doi.org/10.1002/aenm.201702028.

[4] W. Hua, S. Wang, M. Knapp, S.J. Leake, A. Senyshyn, C. Richter, M. Yavuz, J.R. Binder, C.P. Grey, H. Ehrenberg, S. Indris, B. Schwarz, Structural insights into the formation and voltage degradation of lithium- and manganese-rich layered oxides, Nat. Commun. 10 (2019) 1–11. https://doi.org/10.1038/s41467-019-13240-z.

[5] M.M. Thackeray, J.R. Croy, E. Lee, A. Gutierrez, M. He, J.S. Park, B.T. Yonemoto, B.R. Long, J.D. Blauwkamp, C.S. Johnson, Y. Shin, W.I.F. David, The quest for manganese-rich electrodes for lithium batteries: Strategic design and electrochemical behavior, Sustain. Energy Fuels. 2 (2018) 1375–1397. https://doi.org/10.1039/c8se00157j.

[6] M.M. Thackeray, M.F. Mansuetto, D.W. Dees, D.R. Vissers, The thermal stability of

lithium-manganese-oxide spinel phases, Mater. Res. Bull. 31 (1996) 133–140. https://doi.org/10.1016/0025-5408(95)00190-5.

[7] J. Abou-Rjeily, I. Bezza, N.A. Laziz, C. Autret-Lambert, M.T. Sougrati, F. Ghamouss, High-rate cyclability and stability of LiMn2O4 cathode materials for lithium-ion batteries from low-cost natural β−MnO2, Energy Storage Mater. 26 (2020) 423–432. https://doi.org/10.1016/j.ensm.2019.11.015.

[8] J. Zhang, X. Guo, S. Yao, X. Qiu, High capacity lithium-manganese-nickel-oxide composite cathodes with low irreversible capacity loss and good cycle life for lithium ion batteries, Sci. China Chem. 59 (2016) 1479–1485. https://doi.org/10.1007/s11426-016-0109-1.

[9] Y. Hu, Y. Wu, J. Wang, Manganese-Oxide-Based Electrode Materials for Energy Storage Applications: How Close Are We to the Theoretical Capacitance?, Adv. Mater. 30 (2018) 1–21. https://doi.org/10.1002/adma.201802569.

[10] H. Pan, S. Zhang, J. Chen, M. Gao, Y. Liu, T. Zhu, Y. Jiang, Li- and Mn-rich layered oxide cathode materials for lithium-ion batteries: A review from fundamentals to research progress and applications, Mol. Syst. Des. Eng. 3 (2018) 748–803. https://doi.org/10.1039/c8me00025e.

[11] R.C. Longo, F.T. Kong, K.C. Santosh, M.S. Park, J. Yoon, D.H. Yeon, J.H. Park, S.G. Doo, K. Cho, Phase stability of Li-Mn-O oxides as cathode materials for Li-ion batteries: Insights from ab initio calculations, Phys. Chem. Chem. Phys. 16 (2014) 11233–11242. https://doi.org/10.1039/c4cp00937a.

[12] J.R. Croy, A. Gutierrez, M. He, B.T. Yonemoto, E. Lee, M.M. Thackeray, Development of manganese-rich cathodes as alternatives to nickel-rich chemistries, J. Power Sources.

434 (2019) 226706. https://doi.org/10.1016/j.jpowsour.2019.226706.

[13] C.Z. 1 Qiming Liu 1, Huali Zhu 2 , Jun Liu 1, Xiongwei Liao 1, Zhuolin Tang 1, L.L. 1 and Z.C. 1 Mengming Yuan 1, Junfei Duan 1, High-Performance Lithium-Rich Layered Oxide Material: Effects of Preparation Methods on Microstructure and Electrochemical Properties, Materials (Basel). 13 (2020). https://www.mendeley.com/catalogue/2f474463-881c-3a5d-8bb3-277600973b75/?utm_source=desktop&utm_medium=1.19.8&utm_campaign=open_catalog&userDocumentId=%7Bb068cefc-36f1-4d36-95df-f049e647cd45%7D.

[14] S. Li, X. Fu, Y. Liang, S. Wang, X. Zhou, H. Dong, K. Tuo, C. Gao, X. Cui, Enhanced Structural Stability of Boron-Doped Layered@Spinel@Carbon Heterostructured Lithium-Rich Manganese-Based Cathode Materials, ACS Sustain. Chem. Eng. 8 (2020) 9311–9324. https://doi.org/10.1021/acssuschemeng.0c00870.

[15] J. Liu, Q. Liu, H. Zhu, F. Lin, Y. Ji, B. Li, J. Duan, L. Li, Z. Chen, Effect of different composition on voltage attenuation of Li-rich cathode material for lithium-ion batteries, Materials (Basel). 13 (2020). https://doi.org/10.3390/ma13010040.

[16] Z. Ogumi, K. Miyazaki, Fuel Cells - Direct Alcohol Fuel Cells | Direct Ethylene Glycol Fuel Cells, Encycl. Electrochem. Power Sources. (2009) 412–419. https://doi.org/10.1016/B978-044452745-5.00881-9.

[17] Y. Xiang, J. Li, Q. Liao, X. Wu, Morphology and particle growth of Mn-based carbonate precursor in the presence of ethylene glycol for high-capacity Li-rich cathode materials, Ionics (Kiel). 25 (2019) 81–87. https://doi.org/10.1007/s11581-018-2569-4.

[18] T. Lazarova, M. Georgieva, D. Tzankov, D. Voykova, L. Aleksandrov, Z. Cherkezova-Zheleva, D. Kovacheva, Influence of the type of fuel used for the solution combustion

synthesis on the structure, morphology and magnetic properties of nanosized NiFe2O4, J. Alloys Compd. 700 (2017) 272–283. https://doi.org/10.1016/j.jallcom.2017.01.055.

[19] Y. Cai, L. Ku, L. Wang, Y. Ma, H. Zheng, W. Xu, J. Han, B. Qu, Y. Chen, Q. Xie, D.L. Peng, Engineering oxygen vacancies in hierarchically Li-rich layered oxide porous microspheres for high-rate lithium ion battery cathode, Sci. China Mater. 62 (2019) 1374–1384. https://doi.org/10.1007/s40843-019-9456-1.

[20] L. Zhang, K. Jin, L. Wang, Y. Zhang, X. Li, Y. Song, High capacity Li1.2Mn0.54Ni0.13Co0.13O2 cathode materials synthesized using mesocrystal precursors for lithium-ion batteries, J. Alloys Compd. 638 (2015) 298–304. https://doi.org/10.1016/j.jallcom.2015.03.100.

[21] Y. Pei, C.Y. Xu, Y.C. Xiao, Q. Chen, B. Huang, B. Li, S. Li, L. Zhen, G. Cao, Phase Transition Induced Synthesis of Layered/Spinel Heterostructure with Enhanced Electrochemical Properties, Adv. Funct. Mater. 27 (2017). https://doi.org/10.1002/adfm.201604349.

[22] J. Reed, G. Ceder, A. Van Der Ven, Layered-to-spinel phase transition in LixMnO2, Electrochem. Solid-State Lett. 4 (2001) 78–81. https://doi.org/10.1149/1.1368896.

[23] G. Sun, X. Yin, W. Yang, A. Song, C. Jia, W. Yang, Q. Du, Z. Ma, G. Shao, The effect of cation mixing controlled by thermal treatment duration on the electrochemical stability of lithium transition-metal oxides, Phys. Chem. Chem. Phys. 19 (2017) 29886–29894. https://doi.org/10.1039/c7cp05530g.

[24] R.E. Ruther, A.F. Callender, H. Zhou, S.K. Martha, J. Nanda, Raman Microscopy of Lithium-Manganese-Rich Transition Metal Oxide Cathodes, J. Electrochem. Soc. 162 (2015) A98–A102. https://doi.org/10.1149/2.0361501jes.

[25] V. Krishnamoorthy, S. V. Pisupati, Effect of temperature, pressure, feed particle size, and feed particle density on structural characteristics and reactivity of chars generated during gasification of pittsburgh No.8 coal in a high-pressure, high-temperature flow reactor, Energies. 12 (2019) 1–27. https://doi.org/10.3390/en12244773.

[26] R.A.E. Acedera, G. Gupta, M. Mamlouk, M.D.L. Balela, Solution combustion synthesis of porous Co3O4 nanoparticles as oxygen evolution reaction (OER) electrocatalysts in alkaline medium, J. Alloys Compd. 836 (2020) 154919. https://doi.org/10.1016/j.jallcom.2020.154919.

[27] A. Hassanzadegan, G. Blöcher, H. Milsch, L. Urpi, G. Zimmermann, The effects of temperature and pressure on the porosity evolution of flechtinger sandstone, Rock Mech. Rock Eng. 47 (2014) 421–434. https://doi.org/10.1007/s00603-013-0401-z.

[28] H. Ronduda, M. Zybert, A. Szczęsna-Chrzan, T. Trzeciak, A. Ostrowski, D. Szymański, W. Wieczorek, W. Raróg-Pilecka, M. Marcinek, On the sensitivity of the ni-rich layered cathode materials for li-ion batteries to the different calcination conditions, Nanomaterials. 10 (2020) 1–21. https://doi.org/10.3390/nano10102018.

[29] Y. Wang, J. Roller, R. Maric, Morphology-Controlled One-Step Synthesis of Nanostructured LiNi1/3Mn1/3Co1/3O2 Electrodes for Li-Ion Batteries, ACS Omega. 3 (2018) 3966–3973. https://doi.org/10.1021/acsomega.8b00380.

[30] Y. Song, L. Li, Y. Wang, C. Wang, Z. Guo, Y. Xia, Nitrogen-doped ordered mesoporous carbon with a high surface area, synthesized through organic-inorganic coassembly, and its application in supercapacitors, ChemPhysChem. 15 (2014) 2084–2093. https://doi.org/10.1002/cphc.201402250.

[31] A.P. Grosvenor, M.C. Biesinger, R.S.C. Smart, N.S. McIntyre, New interpretations of

XPS spectra of nickel metal and oxides, Surf. Sci. 600 (2006) 1771–1779. https://doi.org/10.1016/j.susc.2006.01.041.

[32] P. Salunkhe, A. V. Muhammed Ali, D. Kekuda, Investigation on tailoring physical properties of Nickel Oxide thin films grown by dc magnetron sputtering, Mater. Res. Express. 7 (2020). https://doi.org/10.1088/2053-1591/ab69c5.

[33] T.E. Jones, T.C.R. Rocha, A. Knop-Gericke, C. Stampfl, R. Schlögl, S. Piccinin, Thermodynamic and spectroscopic properties of oxygen on silver under an oxygen atmosphere, Phys. Chem. Chem. Phys. 17 (2015) 9288–9312. https://doi.org/10.1039/c5cp00342c.

[34] J. Wu, Z. Zhuo, X. Rong, K. Dai, Z. Lebens-Higgins, S. Sallis, F. Pan, L.F.J. Piper, G. Liu, Y. de Chuang, Z. Hussain, Q. Li, R. Zeng, Z. xun Shen, W. Yang, Dissociate lattice oxygen redox reactions from capacity and voltage drops of battery electrodes, Sci. Adv. 6 (2020) 1–12. https://doi.org/10.1126/sciadv.aaw3871.

[35] H. Yu, H. Zhou, High-energy cathode materials (Li2MnO3-LiMO 2) for lithium-ion batteries, J. Phys. Chem. Lett. 4 (2013) 1268–1280. https://doi.org/10.1021/jz400032v.

[36] F. Sigel, B. Schwarz, K. Kleiner, C. Dräger, L. Esmezjan, M. Yavuz, S. Indris, H. Ehrenberg, Thermally Induced Structural Reordering in Li- And Mn-Rich Layered Oxide Li Ion Cathode Materials, Chem. Mater. 32 (2020) 1210–1223. https://doi.org/10.1021/acs.chemmater.9b04355.

[37] H. Li, X. Wei, P. Yang, Y. Ren, S. Wang, Y. Xing, S. Zhang, Uniform Li1.2Ni0.13Co0.13Mn0.54O2 hollow microspheres with improved electrochemical performance by a facile solvothermal method for lithium ion batteries, Electrochim. Acta. 261 (2018) 86–95. https://doi.org/10.1016/j.electacta.2017.10.119.

[38] J. Li, C. Xu, J. Zhao, J. Chen, C. Cao, Li-rich nanoplates of Li1.2Ni0.13Co0.13Mn0.54O2 layered oxide with exposed {010} planes as a high-performance cathode for lithium-ion batteries, J. Alloys Compd. 734 (2018) 301–306. https://doi.org/10.1016/j.jallcom.2017.10.285.

[39] Y. Di Zhang, Y. Li, X.Q. Niu, D.H. Wang, D. Zhou, X.L. Wang, C.D. Gu, J.P. Tu, A peanut-like hierarchical micro/nano-Li1.2Mn0.54Ni0.18Co0.08O2 cathode material for lithium-ion batteries with enhanced electrochemical performance, J. Mater. Chem. A. 3 (2015) 14291–14297. https://doi.org/10.1039/c5ta02915e.

[40] J. Li, T. Jia, K. Liu, J. Zhao, J. Chen, C. Cao, Facile design and synthesis of Li-rich nanoplates cathodes with habit-tuned crystal for lithium ion batteries, J. Power Sources. 333 (2016) 37–42. https://doi.org/10.1016/j.jpowsour.2016.09.150.

[41] S. Shi, S. Zhang, Z. Wu, T. Wang, J. Zong, M. Zhao, G. Yang, Full microwave synthesis of advanced Li-rich manganese based cathode material for lithium ion batteries, J. Power Sources. 337 (2017) 82–91. https://doi.org/10.1016/j.jpowsour.2016.10.107.

[42] S. Shi, T. Wang, M. Cao, J. Wang, M. Zhao, G. Yang, Rapid Self-Assembly Spherical Li1.2Mn0.56Ni0.16Co0.08O2 with Improved Performances by Microwave Hydrothermal Method as Cathode for Lithium-Ion Batteries, ACS Appl. Mater. Interfaces. 8 (2016) 11476–11487. https://doi.org/10.1021/acsami.6b01683.

[43] Y. Zhang, W. Zhang, S. Shen, X. Yan, A. Wu, J. Yin, J. Zhang, Hollow porous bowl-shaped lithium-rich cathode material for lithium-ion batteries with exceptional rate capability and stability, J. Power Sources. 380 (2018) 164–173. https://doi.org/10.1016/j.jpowsour.2018.01.084.

[44] L. Nation, Y. Wu, C. James, Y. Qi, B.R. Powell, B.W. Sheldon, Si-doped high-energy

Li1.2Mn0.54Ni0.13Co0.13O2 cathode with improved capacity for lithium-ion batteries, J. Mater. Res. 33 (2018) 4182–4191. https://doi.org/10.1557/jmr.2018.378.

[45] Z. Lu, J.R. Dahn, Understanding the Anomalous Capacity of Li/Li[Ni[sub x]Li[sub (1/3−2x/3)]Mn[sub (2/3−x/3)]]O[sub 2] Cells Using In Situ X-Ray Diffraction and Electrochemical Studies, J. Electrochem. Soc. 149 (2002) A815. https://doi.org/10.1149/1.1480014.

[46] S. Dou, F. Wei, H. Li, P. Li, Cobalt-free Li-Rich 0.1Li2MnO3•0.9LiNi0.56Mn0.44O2 with High Performances as Cathode Material for Lithium-ion Batteries, IOP Conf. Ser. Mater. Sci. Eng. 381 (2018) 0–10. https://doi.org/10.1088/1757-899X/381/1/012180.

Figures

Scheme1: Representation of equation between ethylene glycol and metal oxides.

Scheme 2: Schematic diagram for the incorporating oxygen vacancies into LNMO cathode material.

Figure 1: Structural representation of (a) $LiMO_2$ layered oxides, (b) the overall cell of Li-rich layered oxides described as monoclinic and (c) $LiMnO_2$ layered pattern leading to honeycomb pattern.

Figure 2: Representation of XRD patterns of Li $[Li_{0.1} Ni_{0.3} Mn_{0.7}] O_2$ calcinated at three different temperatures.

Figure 3: Representation of Raman Spectra of Li $[Li_{0.1} Ni_{0.3} Mn_{0.7}] O_2$ calcinated at three different temperatures.

Figure 4: a) b) Representation of FE-SEM images of Li $[Li_{0.1} Ni_{0.3} Mn_{0.7}] O_2$ calcinated at 900 ^{o} C, at different locations. (c) EDX spectrum of Li $[Li_{0.1} Ni_{0.3} Mn_{0.7}] O_2$ calcinated at 900 ^{o} C.

Figure 5: Representation of XPS Spectra of Li $[Li_{0.1} Ni_{0.3} Mn_{0.7}] O_2$: a) Mn 2p, b) Ni 2p, c) Li^{+}, d) O 1s calcinated at 900 ^{o} C.

Figure 6: Representation of Electrochemical performance of Li $[Li_{0.1} Ni_{0.3} Mn_{0.7}] O_2$: at a) 600^{o} C, b) 750^{o} C, c) 900^{o} C, d) Cyclic performance of Li $[Li_{0.1} Ni_{0.3} Mn_{0.7}] O_2$ at different temperatures.

Figure 7: Representation of **(a)** Rate performance of Li $[Li_{0.1} Ni_{0.3} Mn_{0.7}] O_2$ at 900 ^{o} C, (b) Cyclic Voltammograms of Li $[Li_{0.1} Ni_{0.3} Mn_{0.7}] O_2$ treated at different temperatures.

(c) Representation of Ac Impedance Spectroscopy of Li [Li $_{0.1}$ Ni $_{0.3}$ Mn $_{0.7}$] O_2 at different temperatures.

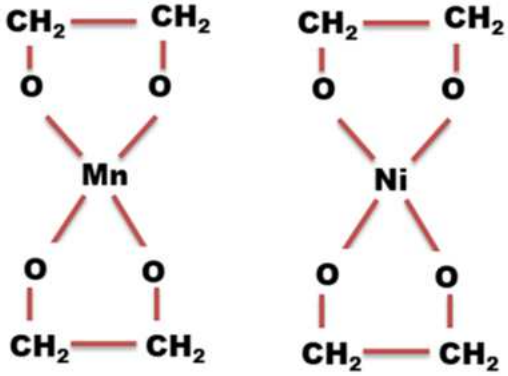

Scheme1: Representation of equation between ethylene glycol and metal oxides.

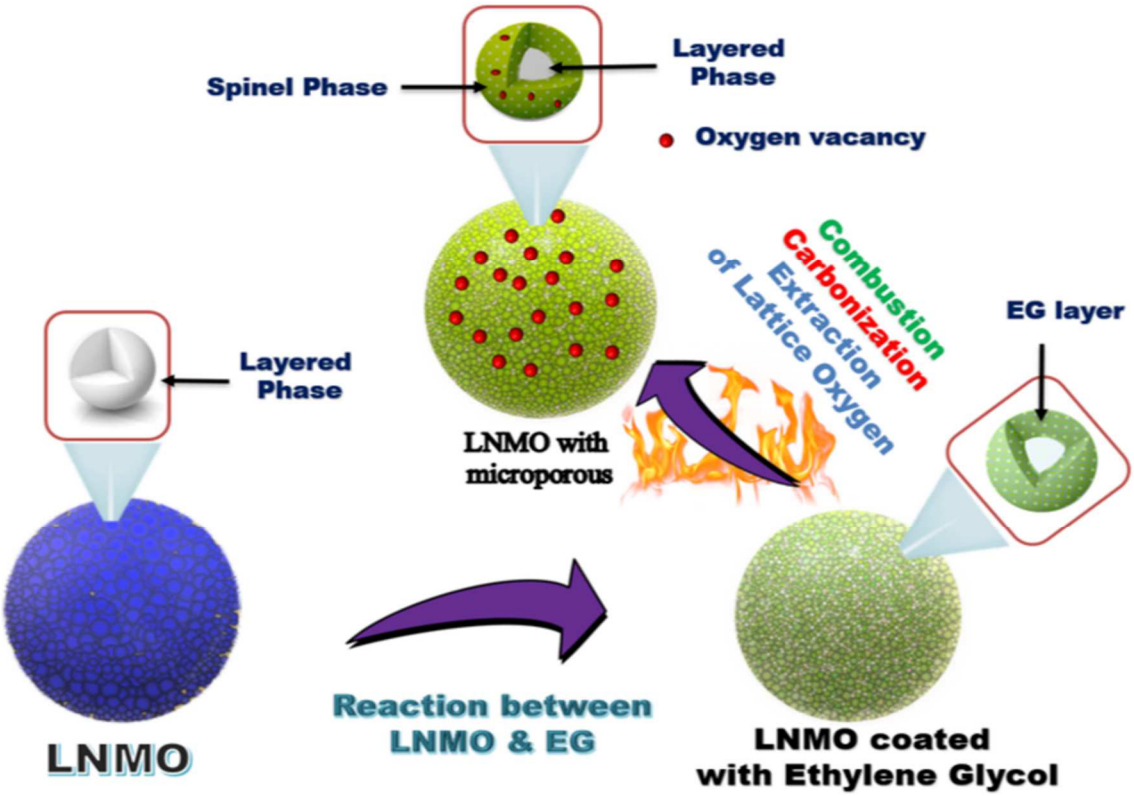

Scheme 2: Schematic diagram for the incorporating oxygen vacancies into LNMO cathode material

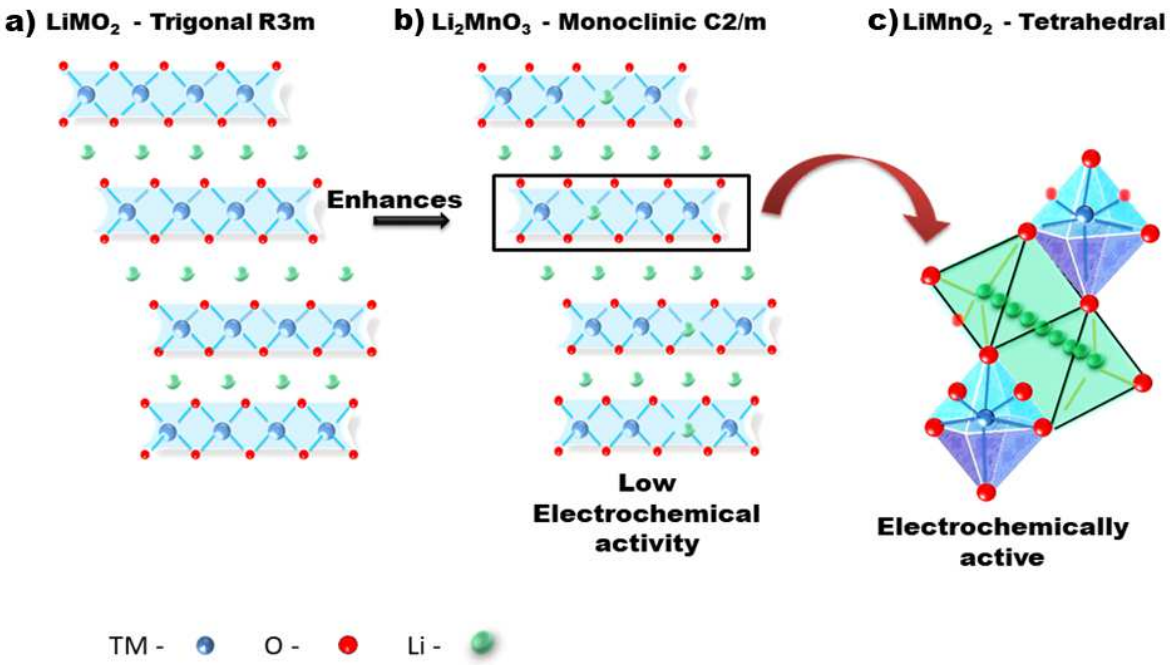

Figure 1: Structural representation of (a) $LiMO_2$ layered oxides, (b) the overall cell of Li-rich layered oxides described as monoclinic and (c) $LiMnO_2$ layered pattern leading to honeycomb pattern.

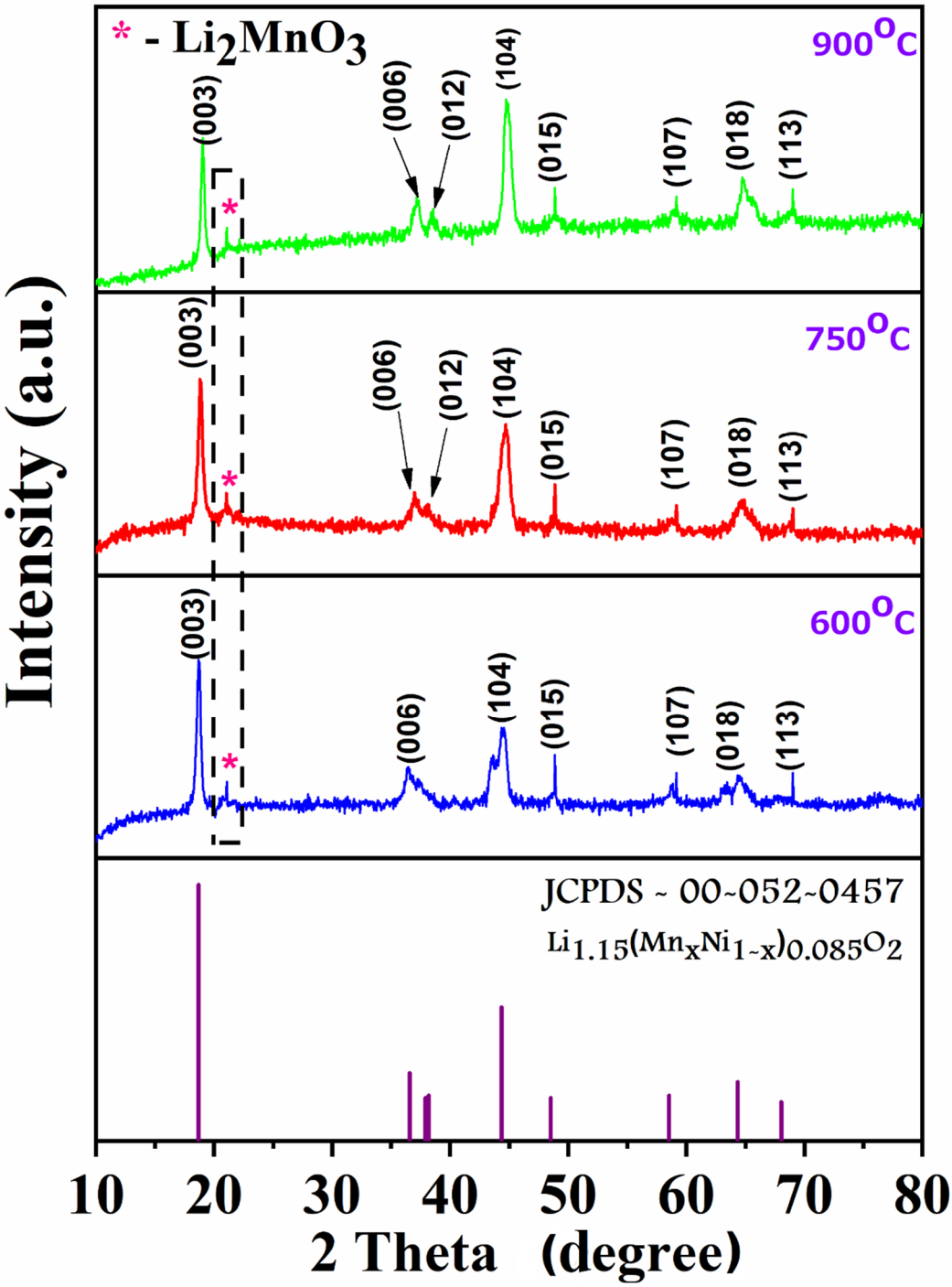

Figure 2: Representation of XRD patterns of Li [Li $_{0.1}$ Ni $_{0.3}$ Mn $_{0.7}$] O_2 calcinated at three different temperatures.

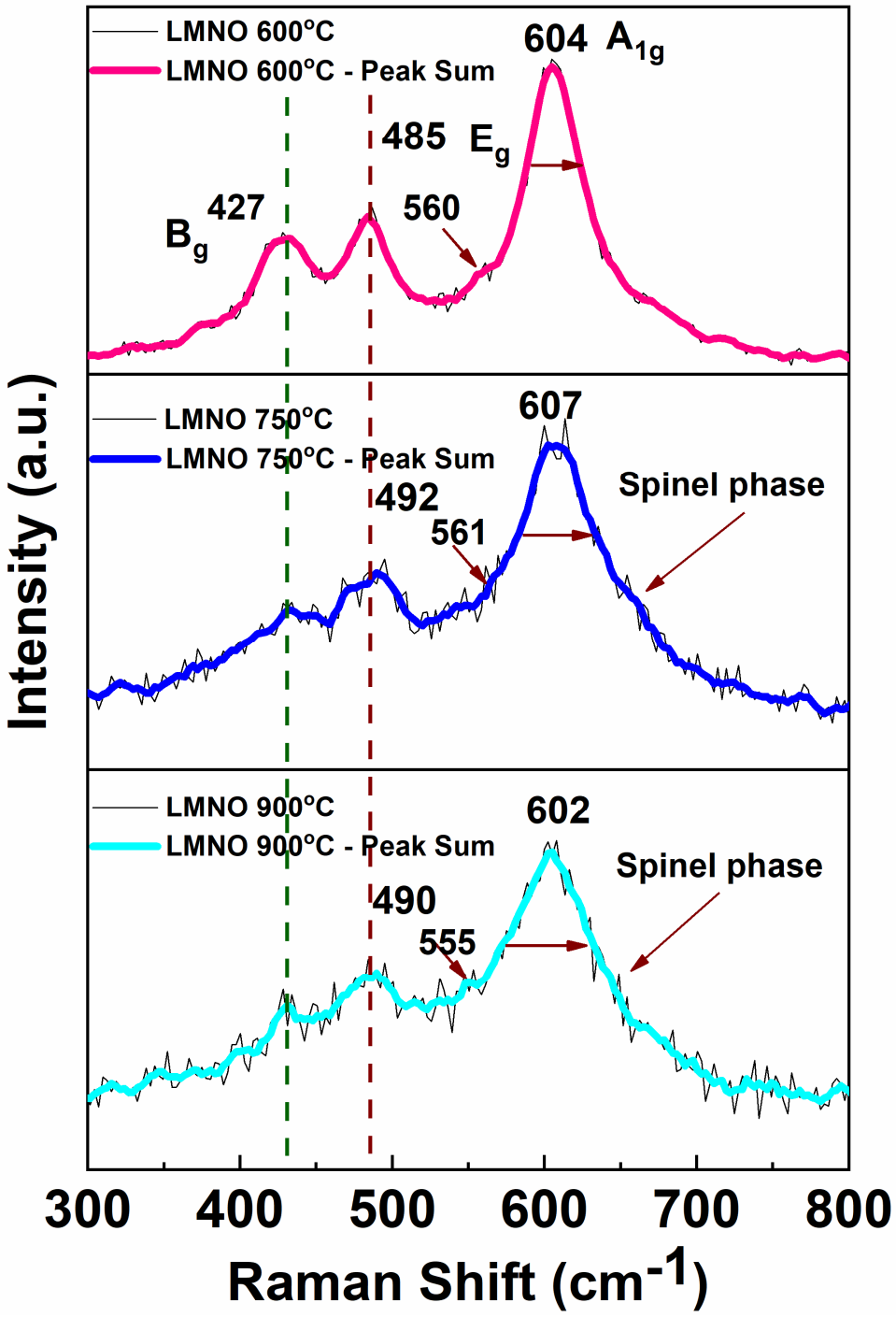

Figure 3: Representation of Raman Spectra of Li $[Li_{0.1} Ni_{0.3} Mn_{0.7}] O_2$ calcinated at three different temperatures.

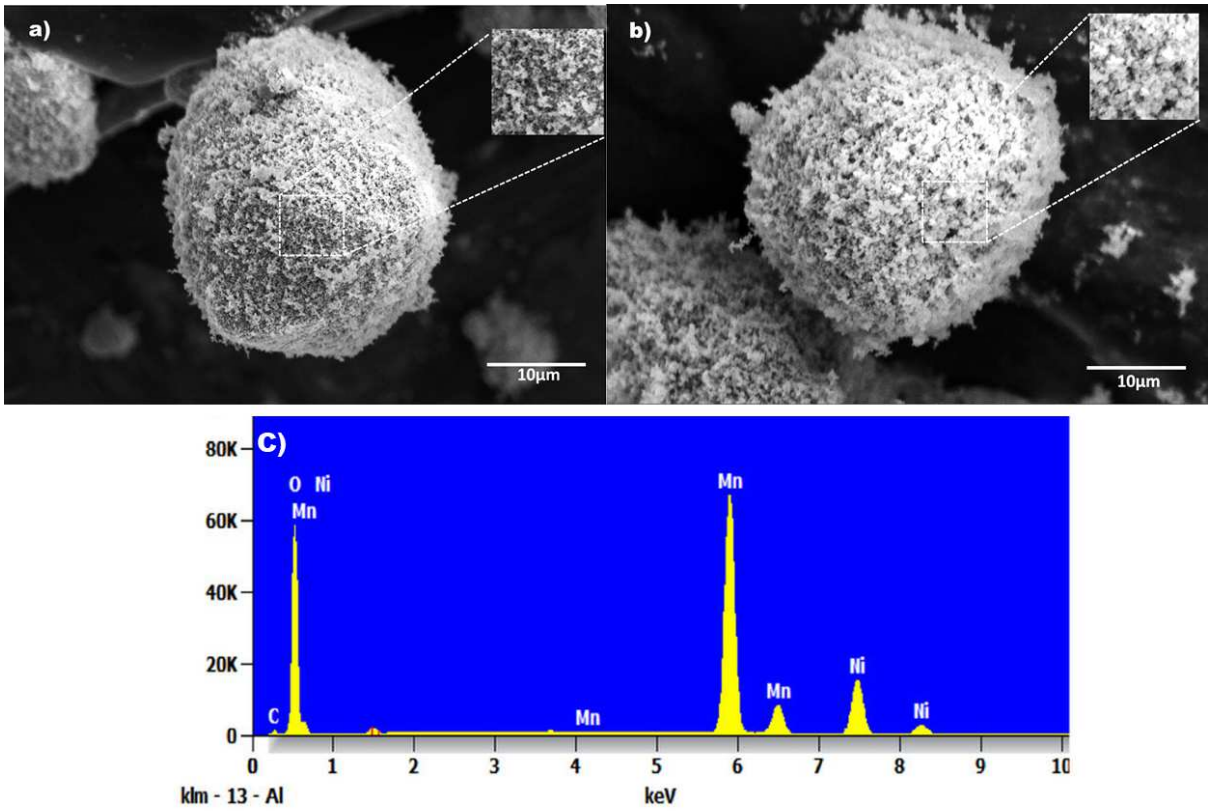

Figure 4: (a), (b) Representation of FE-SEM images of Li [Li $_{0.1}$ Ni $_{0.3}$ Mn $_{0.7}$] O_2 calcinated at 900^o C at different locations. (c) EDX spectrum of Li [Li $_{0.1}$ Ni $_{0.3}$ Mn $_{0.7}$] O_2 calcinated at 900^o C.

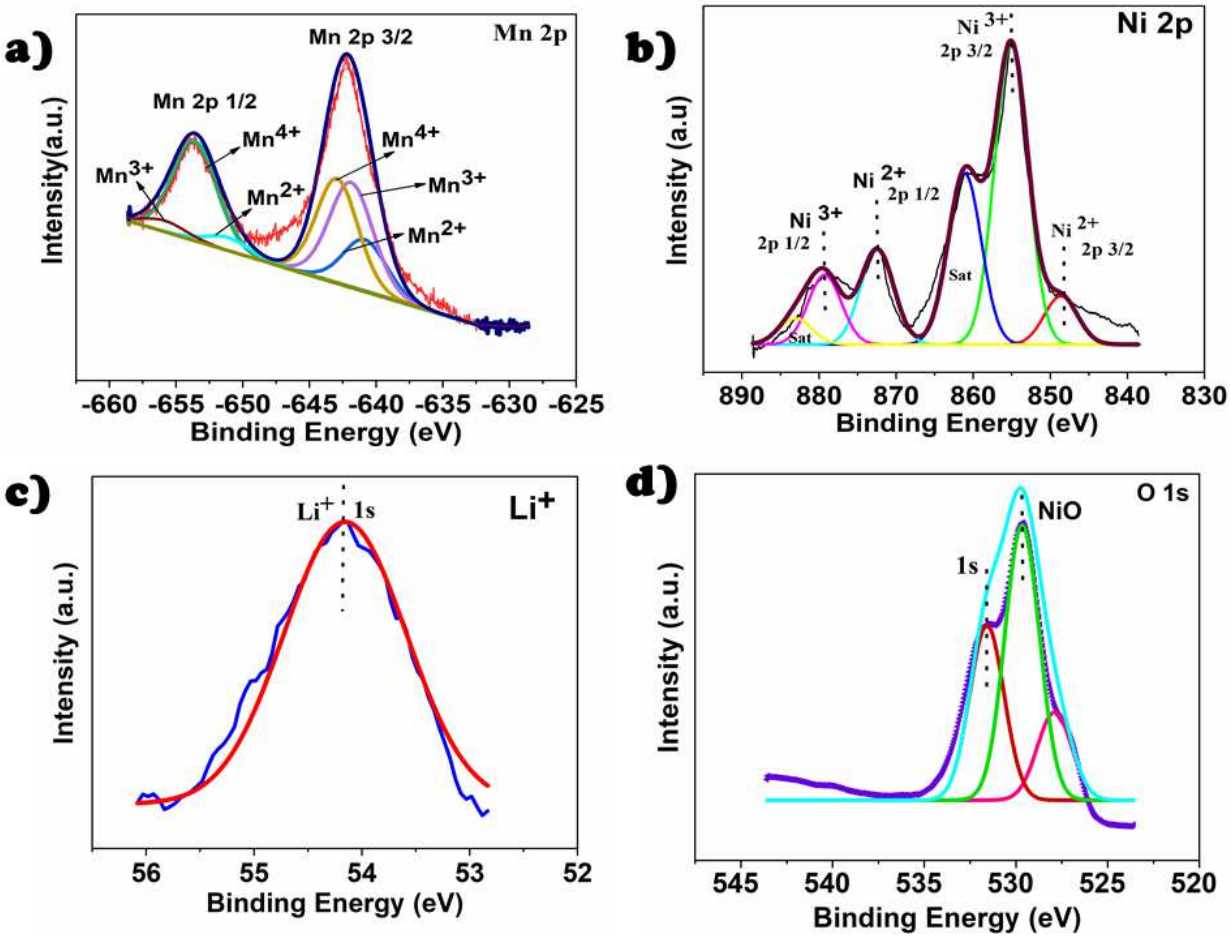

Figure 5: Representation of XPS Spectra of Li [Li $_{0.1}$ Ni $_{0.3}$ Mn $_{0.7}$] O_2: a) Mn 2p, b) Ni 2p, c) Li^+, d) O 1s calcinated at 900^o C.

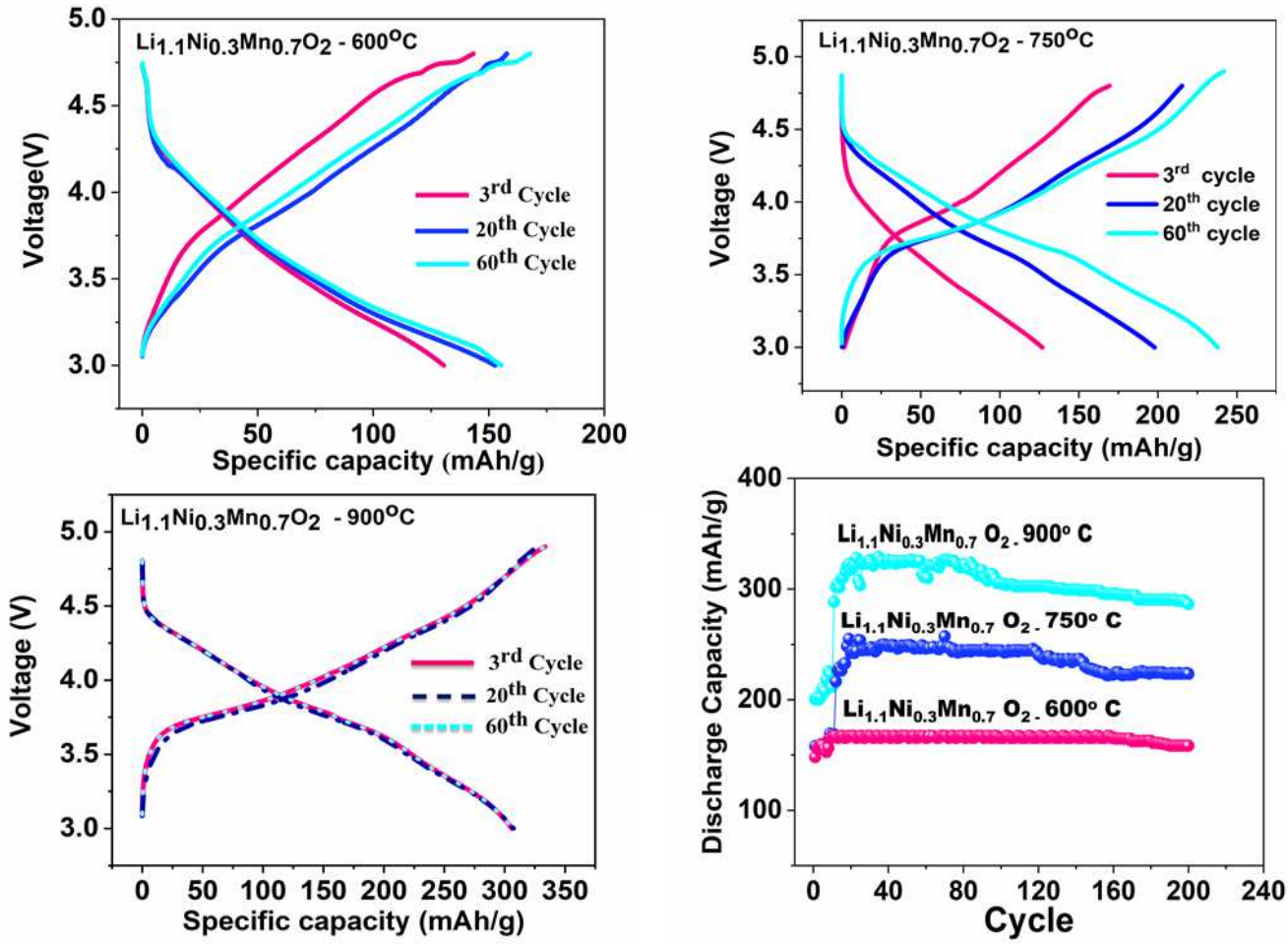

Figure 6: Representation of Electrochemical performance of Li [Li $_{0.1}$ Ni $_{0.3}$ Mn $_{0.7}$] $O_{2:}$ at

a) 600° C, b) 750° C, c) 900° C,

d) Cyclic performance of Li [Li $_{0.1}$ Ni $_{0.3}$ Mn $_{0.7}$] O_2 at different temperatures.

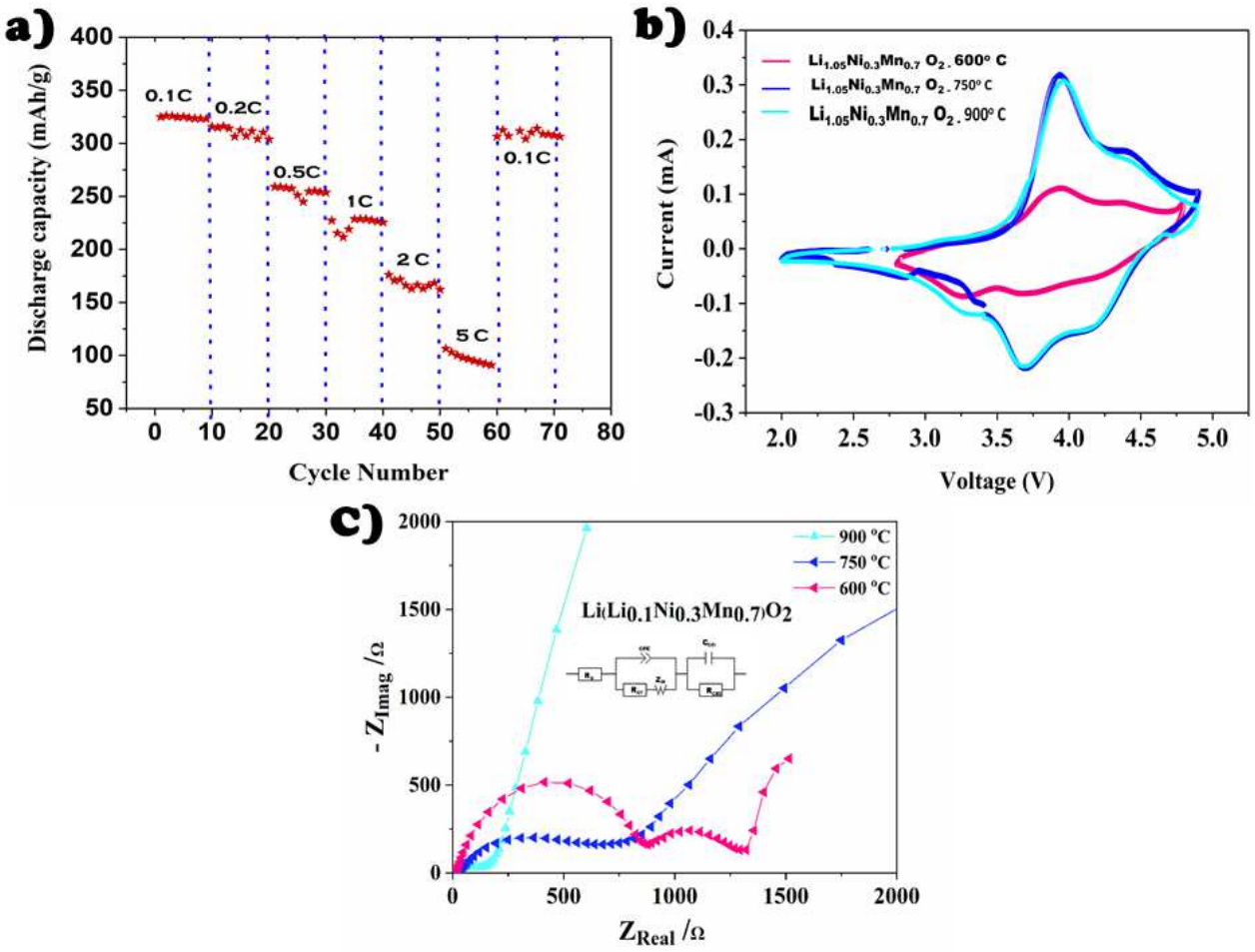

Figure 7: Representation of **(a)** Rate performance of Li [Li $_{0.1}$ Ni $_{0.3}$ Mn $_{0.7}$] O_2 at 900 ^{o} C, (b) Cyclic Voltammograms of Li [Li $_{0.1}$ Ni $_{0.3}$ Mn $_{0.7}$] O_2 treated at different temperatures. (c) Representation of Ac Impedance Spectroscopy of Li [Li $_{0.1}$ Ni $_{0.3}$ Mn $_{0.7}$] O_2 at different temperatures.

Table 1. The lattice parameters are calculated using XRDA software

Temperature **^{o}C**	**a = b** **Å**	**c** **Å**	**c/a** **Å**	**I(003)/I(104)**
600 ^{o}C	2.8709	14.336	4.9935	1.22
750 ^{o}C	2.870	14.323	4.9908	1.200
900 ^{o}C	2.866	14.288	4.9853	0.8345
JCPDS - 00-052-0457	2.8777	14.2220	4.9453	

Table 2: BET characterisation results for Li $[Li_{0.1} Ni_{0.3} Mn_{0.7}] O_2$ at different temperatures

Samples	**(S_{BET})** **(m2 g –1)**	**(V_P)** **(cm3 g –1)**	**(D_P)** **(nm)**
600 ^{o}C	**9.7**	**0.023**	**3.236**
750 ^{o}C	**15.1**	**0.048**	**5.68**
900 ^{o}C	**15.4**	**0.053**	**6.31**

S_{BET} - BET surface area, V_P - Pore volume, D_P -Mean pore diameter

Table 3: Comparison of electrochemical performance of the Li $[Li_{0.1} Ni_{0.3} Mn_{0.7}] O_2$ with previously reported LMRO cathode or similar compositions

Synthesis technique	Structure & Morphology	Specific capacity (mhA/g)	Capacity Retention & Ref
1. Facile Solvothermal	Hollow microspheres	150	81.3% (After 100 cycles)[37]
2. PVP- assisted Co- precipitation @ N2	Nanoplates	139.2	88.2% (After 100 cycles)[38]
3. Facile Solvothermal combined with calcination process	Peanut- like structure	167.5	94.2% (After 100 cycles)[39]
4. Facile Synthesis	Nano plates with {010}	113.8	79.5 % (After 100 cycles)[40]
5. Full microwave synthesis	Spherical hierarchical	192.5	83.3[41] (After 100 cycles)
6. Microwave Hydrothermal	Self-assembly Spherical particles	131	80.7[42] (After 100 cycles)
7. PVP- EG assisted Co-precipitation	Hollow porous Bowl shaped	205	92[43] (After 100 cycles)
8. Rapid combustion assisted co-precipitation method	Highly Porous spherical ball	305	94 (After 100 cycles) This work

Table 4: EIS results of Li $[Li_{0.1} Ni_{0.3} Mn_{0.7}] O_2$ at different temperatures

Samples	**600 ºC**	**750 ºC**	**900 ºC**
***Rs* Ω**	**2.743**	**1.817**	**0.862**
Rct Ω	**891.1**	**173.2**	**123.4**
Exchange Current Density (A)	**0.28818×10^{-4}**	**1.4826×10^{-4}**	**2.0810×10^{-4}**

R CEI	**82.33**	**40.76**	**22.42**

***Rct* - Charge transfer resistance, Rs Ω – Resistance of Conducting electrolyte**

Graphical Abstract